Is HE 0436–4717 Anemic? A deep look at a bare Seyfert 1 galaxy

K. Bonson,[1][★] L. C. Gallo[1][★] and R. Vasudevan[2]

[1]*Department of Astronomy and Physics, Saint Mary's University, 923 Robie Street, Halifax, NS B3H 3C3, Canada*
[2]*Institute of Astronomy, Madingley Road, Cambridge CB3 0HA, UK*

ABSTRACT

A multi-epoch, multi-instrument analysis of the Seyfert 1 galaxy HE 0436–4717 is conducted using optical to X-ray data from *XMM–Newton* and *Swift* (including the Burst Alert Telescope). Fitting of the UV-to-X-ray spectral energy distribution shows little evidence of extinction and the X-ray spectral analysis does not confirm previous reports of deep absorption edges from O VIII. HE 0436–4717 is a 'bare' Seyfert with negligible line-of-sight absorption making it ideal to study the central X-ray emitting region. Three scenarios were considered to describe the X-ray data: partial covering absorption, blurred reflection, and soft Comptonization. All three interpretations describe the 0.5–10.0 keV spectra well. Extrapolating the models to 100 keV results in poorer fits for the partial covering model. When also considering the rapid variability during one of the *XMM–Newton* observations, the blurred reflection model appears to describe all the observations in the most self-consistent manner. If adopted, the blurred reflection model requires a very low iron abundance in HE 0436–4717. We consider the possibilities that this is an artefact of the fitting process, but it appears possible that it is intrinsic to the object.

Key words: galaxies: active – galaxies: individual: HE 0436–4717 – galaxies: nuclei – galaxies: Seyfert – X-rays: galaxies.

1 INTRODUCTION

Seyfert 1 galaxies are a subclass of active galactic nuclei (AGN) that provide a preferred view of the central engine. Seyfert 1 galaxies that appear to have little to no intrinsic absorption, so-called 'bare' Seyfert 1s, provide an especially unobscured line of sight to the innermost regions close to the supermassive black hole itself. Such AGN have been noted before (e.g. Vaughan et al. 2004; Emmanoulopoulos et al. 2011) and recently have become the subject of larger sample studies (Patrick et al. 2011; Jin, Ward & Done 2012; Walton et al. 2013).

HE 0436–4717 appears at first to be a rather typical Seyfert 1 galaxy at $z = 0.053$ first observed by the Einstein Slew Survey in 1992 (ESS; Elvis et al. 1992). It has been included in numerous surveys and catalogues since the ESS including: the *ROSAT* All-Sky Survey (Grupe et al. 1998), the Hamburg/ESO Survey for bright QSOs (Wisotzki et al. 2000), and the Palermo *Swift* BAT Hard X-ray Catalogue (Cusumano et al. 2010). Despite its frequent inclusion in such wide-field studies, HE 0436–4717 has been the subject of deep X-ray analysis only once (Wang et al. 1998).

Halpern & Marshall (1996) monitored the object in the extreme UV with the *EUVE* satellite for 20 continuous days and were able to produce a long light curve. The timing analysis of the light curve revealed possible flaring with a period of about 0.9 d. In addition, the authors also analysed spectra from *EUVE*'s short-wavelength spectrometer and found no emission line features in the 70–110 Å range. The column density listed in that work is comparable to Galactic extinction alone, indicating no intrinsic extinction in the object was observed.

A detailed X-ray analysis of this object was done by Wang et al. (1998) using data from *ASCA* and *ROSAT* observations. The authors found the 0.4–10.0 keV spectrum was well modelled by a single power law with slope of $\Gamma = 2.65 \pm 0.20$ or by a sum of a $\Gamma = 2.15 \pm 0.04$ power law and a weak blackbody of temperature 29.0 ± 2.0 eV. The authors describe an Fe Kα emission feature with an equivalent width of around 430 eV and two absorption edges: one at $E \sim 0.28$ keV with an optical depth of $\tau \sim 3.46$ measured from the *ROSAT* spectrum, and one at $E \sim 0.83$ keV with $\tau \sim 0.26$ from the *ASCA* spectra – the latter of which was attributed to a combination of O VII and O VIII edges. A comparison between *ASCA* observations four months apart saw a 47 per cent flux change, however all other spectral parameters remained constant.

In this study, an analysis of HE 0436–4717 multi-epoch data from *XMM–Newton* and *Swift* observatories spanning from 2002 to 2013 is presented. *Chandra* also serendipitously observed this object between 2000 and 2006; however, these data were determined to be piled up and were not used in the analysis (see Section 2.2). The study of *XMM–Newton* and *Swift* data presented here is the deepest investigation of this object to date using the most current instruments and analysis tools.

★ E-mail: kbonson@ap.smu.ca (KB); lgallo@ap.smu.ca (LCW)

Following this introduction, Section 2 describes the data processing for each observation. An initial X-ray spectral analysis of the *XMM–Newton* EPIC data is described in Section 3, including a search for absorption features seen previously in this object. The spectral analysis was extended into the UV band in Section 4, which includes spectral energy distribution (SED) modelling using *Swift* data (UVOT, XRT, and BAT). Section 5 describes an in-depth X-ray analysis of the *XMM–Newton* MOS spectra considering absorption (Section 5.1), reflection (Section 5.3), and soft Comptonization (Section 5.4) scenarios. Section 6 details the timing analysis of the *XMM–Newton* light curves and specifically examines hardness ratios (HR, Section 6.1), fractional variability (Section 6.2), and flux-resolved spectra (Section 6.3). A discussion of the findings (Section 7) and final concluding remarks (Section 8) complete this work.

2 OBSERVATIONS AND DATA REDUCTION

2.1 *XMM–Newton*

XMM–Newton (Jansen et al. 2001) observations of HE 0436–4717 were serendipitous during the targeted observation of the pulsar PSR J0437.4–4711 about 4.2 arcmin away. The first observation (hereafter XMM1) was during revolution 0519 on 2002 October 9 and spanned 70.5 ks. Two MOS detectors (Turner et al. 2001) operated in full-frame mode with the thin filter. Due to the variable nature of the pulsar target, the pn camera (Strüder et al. 2001) was set to timing mode also with a thin filter in place. The Optical Monitor (OM; Mason et al. 2001) simultaneously collected data from HE 0436–4717 during this observation although the object was outside the field of view of the reflection grating spectrometers (den Herder et al. 2001; RGS1 and RGS2). The OM data were limited to observations in the *UVW*1 ($\lambda_{max} = 2675$ Å) and V ($\lambda_{max} = 5235$ Å) filters.

A second *XMM–Newton* observation (hereafter XMM2) was during revolution 1835 on 2009 December 15 and spanned 130 ks. The EPIC instruments operated in the same manner as in XMM1. During XMM2 only the MOS instruments observed HE 0436–4717 as the source fell outside of the pn field of view used for timing mode.

Data files from both epochs were processed to produce calibrated event lists using the *XMM-Newton* Science Analysis System version 12.0.0. The data were examined for background flaring and pileup; only minor flaring was seen in the very beginning of XMM2 and those periods were ignored. No pileup was detected as the source was off-axis and the pn was operated in timing mode. For the MOS data, source photons were extracted from a circular region 35 arcsec in radius and centred on the object. The background photons were extracted from an area 50 arcsec in radius close to the object and then scaled appropriately.

Source photons from the pn data were extracted from a rectangular region 72 arcsec in width centred on the object and the background photons from a larger rectangular region and also scaled. Single-quadruple events were selected for the MOS data while single and double events were selected for the pn; events next to a bad pixel or the CCD edge were omitted (i.e. data quality flag set to zero). The entire process was then repeated for XMM2. The resulting mean count rates were 3.07 count s^{-1} for pn, 1.21 count s^{-1} for MOS1, and 1.29 count s^{-1} for MOS2 in the 0.3–10.0 keV band.

Spectra from the MOS data were limited to the 0.5–10.0 keV range based on cross-calibration uncertainties, while the pn spectra were limited to 0.6–8.0 keV because of the less accurate calibration in timing mode[1] and high background above 8 keV.

2.2 *Chandra*

The pulsar PSR J0437.4–4711 is a calibration source for the *Chandra* observatory. Of the eleven observations between 2000–2006, HE 0436–4717 falls in the field of view during six: ObsIDs 742, 1850, 6155, 6156, 6157, and 7216. ObsIDs 742 and 1850 were observed with the HRC-I and -S detectors and thus only imaging data are available; these were ignored. The ACIS-S data were processed using the most recent version of CIAO at the time (v. 4.4.0) and preliminary spectra were extracted. After analysing the spectra it was clear that the data were piled up. Several reprocessing methods were attempted; however, the quality of the data were not high enough to justify any further analysis.

2.3 *Swift*

HE 0436–4717 has been observed by the *Swift* X-ray Telescope (XRT; Burrows et al. 2005) twice in 2007 and most recently in 2013 June (hereafter Sw3). The first observation (hereafter Sw1) had the highest exposure time, followed by the second observation (hereafter Sw2). Processed Burst Alert Telescope (BAT) spectra and the diagonal response matrix are taken from the *Swift* BAT 70-Month Hard X-ray Survey (Baumgartner et al. 2013). The BAT data are averaged spectra from integration of survey data collected over a 70-month period, whereas the XRT observations are individual exposures of a few kiloseconds during pointed observations (see Table 1).

The XRT observations were performed in photon counting mode. X-ray data were reduced with the XRTPIPELINE version 0.12.1 and spectra were extracted with XSELECT. Optical and UV photometry was obtained with the UV-Optical Telescope (UVOT; Roming et al. 2005). Magnitudes and fluxes were based on the most recent UVOT calibration as described in Poole et al. (2008) and Breeveld et al. (2010).

A summary of the data used in this work is shown in Table 1.

3 PRELIMINARY ANALYSIS OF XMM DATA

All spectral model fitting was performed using the X-ray spectral fitting package XSPEC v. 12.8.1. Model parameters are reported in the rest frame of the AGN ($z = 0.053$) and a cosmology of $H_o = 70$ km s^{-1} Mpc^{-1}, $q_o = 0$, and $\Lambda_o = 0.73$ is assumed. All models include a Galactic column density of $N_H = 1.03 \times 10^{20}$ cm^{-2} as determined from the LAB Survey[2] (Kalberla et al. 2005). Errors on model parameters correspond to a 90 per cent confidence level.

An initial inspection of the *XMM–Newton* EPIC spectra showed consistency between the pn and MOS data for XMM1 and both MOS spectra for XMM2 within known calibration uncertainties. Since the multi-epoch data – for which only MOS data are available – will ultimately be compared, the pn data will not be discussed, although it was continually examined for consistency throughout the study. The MOS 1 and MOS 2 data at each epoch were merged into single spectrum and response file using the FTOOLS

---

[1] See *XMM–Newton* Calibration Technical Note 0018 (XMM-SOC-CAL-TN-0018) section 11.2.2 for details.

[2] http://heasarc.nasa.gov/cgi-bin/Tools/w3nh/w3nh.pl

Table 1. HE 0436–4717 data log.

(1) Telescope	(2) ObsID	(3) Instrument	(4) Filter	(5) Start date	(6) Duration (s)	(7) GTI (s)
XMM–Newton	0112320201	pn	Thin	2002-09-10	68 177	67 210
		MOS 1	Thin		69 167	68 270
		MOS 2	Thin		69 167	68 380
		OM	*UVW*1		34 996*	N/A
			V		25 000*	N/A
	0603460101	MOS 1	Thin	2009-12-15	129 141	126 900
		MOS 2	Thin		129 146	123 600
Swift	00035763001	XRT	None	2007-12-07	10 090	9732
		UVOT	*V*		838	838
			B		840	840
			U		840	840
			*UVW*1		1681	1681
			*UVM*2		2286	2286
			*UVW*2		3369	3369
	70-month survey	BAT	None	2010-09-21	N/A	N/A

Note. *Individual filters exposed for a range of 1998–5001 s each with a sum of ten exposures for *UVW*1 and five exposures for *V*.

program ADDASCASPEC in an effort to increase signal to noise and simplify model fitting.

The merged MOS spectra at each epoch were fit from 2–10 keV with a power law and the model extrapolated to 0.5 keV. The residuals clearly show a soft-excess (SE), common in Seyfert 1 galaxies, and excess residuals around 6.4 keV (second from top panel, Fig. 1). The addition of a blackbody at low energies fit the SE very well leaving only residuals at higher energies (second from bottom, Fig. 1). The addition of a narrow ($\sigma = 1\,\mathrm{eV}$) Gaussian profile at ∼6.4 keV, common at both epochs, improved the fit further but still left significant residuals. Adding a second, broader Gaussian profile ($E \approx 6\,\mathrm{keV}$ and $\sigma \approx 3\,\mathrm{keV}$) improved the quality of fit ($\Delta\chi^2 = 14$ for 3 additional free parameters; Fig. 1, top panel) and residuals (Table 2; Fig. 1, bottom panel). Reversing the order of line fitting – adding a broad Gaussian line first – does not influence the final fit as the fit statistic remained the same (i.e. two Gaussian profiles are still required to reconcile all iron residuals).

The described model provides a good fit to the multi-epoch spectra ($\chi^2_\nu/\mathrm{dof} = 1.07/2025$; Fig. 1 top and bottom panels). Wang et al. (1998) reported an absorption edge around $E \sim 0.83$ keV with $\tau \sim 0.26$ from their analysis of *ASCA* spectra. Including this exact feature in the *XMM–Newton* spectrum degraded the fit (Fig. 2). Allowing the absorption energy and depth to vary did not improve the fit significantly ($\Delta\chi^2 = 11$ for 2 additional free parameters) and the measured edge energy ($E = 0.72 \pm 0.03$) and optical depth ($\tau = 0.06 \pm 0.03$) were inconsistent with the *ASCA* measurements. Likewise, adding an absorber associated with the host galaxy did not enhance the fit and only an upper limit of $N_\mathrm{H} < 10^{19}\,\mathrm{cm}^{-2}$ could be measured. The *XMM–Newton* spectra here do not support significant additional absorption that was reported from the *ASCA* analysis (Wang et al. 1998).

The best-fitting phenomenological model presented in Table 2 does not reveal the physical processes at work in HE 0436–4717. The broad Gaussian profile could be associated with blurred reflection or partial covering absorption. The strength of the SE, defined as the flux ratio between the blackbody and power-law component between 0.4 and 3 keV, could indicate whether the low-energy spectrum is sculpted by absorption or reflection (Vasudevan et al. 2014), but the ratio measured in HE 0436–4717 (SE ≈ 0.1) is
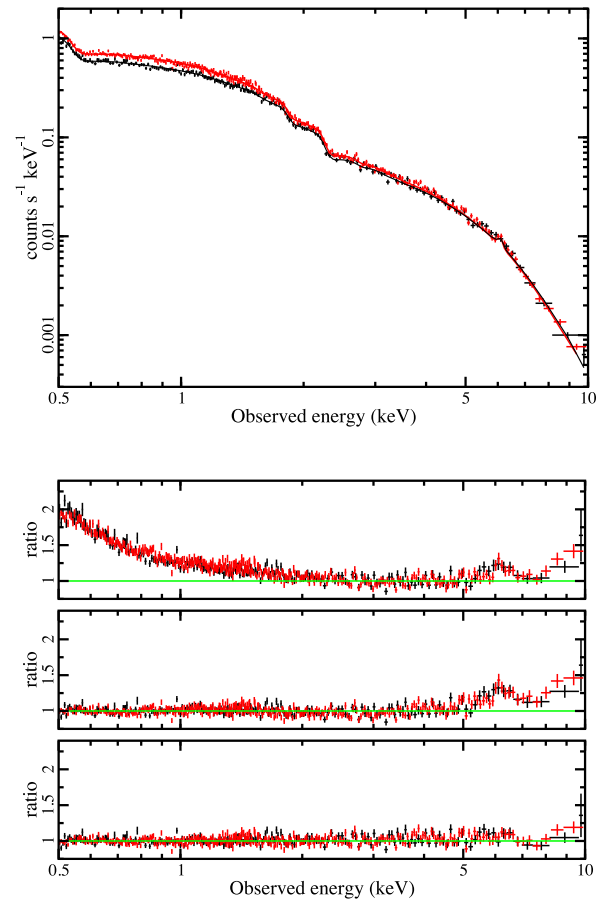

Figure 1. Preliminary analysis of the *XMM–Newton* merged MOS spectra. XMM1 (black) and XMM2 (red) data were fitted with a power law plus blackbody and two Gaussians in the 0.5–10 keV band (top panel). Extrapolating a power-law fit to the 2-10 keV spectra to lower energies shows clearly a SE below about 2 keV and excess residuals around 6.4 keV (second from top). Adding a blackbody accounts for the SE and residuals in the iron band (second panel from bottom). Including a Gaussian profile at about 6.4 keV with variable width reduces the residuals further (bottom panel).

Table 2. The best phenomenological model fit to the merged *XMM–Newton* MOS spectra. The model components and model parameters are listed in columns 1, and 2, respectively. Columns 3 and 4 list the parameter values during the XMM1 epoch and XMM2 epoch, respectively. Fluxes are corrected for Galactic absorption and are reported in units of $\mathrm{erg\,cm^{-2}\,s^{-1}}$. The SE flux is measured between 0.4 and 3.0 keV. Parameters linked across the epochs are denoted by dots and those without errors are frozen at the given values.

| (1) Model component	(2) Model parameter	(3) XMM1	(4) XMM2
Blackbody	kT (eV)	77 ± 6	79 ± 5
	$F_{0.4-3keV}$	$0.68 \pm 0.05 \times 10^{-12}$	$0.72 \pm 0.05 \times 10^{-12}$
Power law	Γ	2.14 ± 0.04	2.23 ± 0.03
	$F_{0.4-3keV}$	$5.36 \pm 0.05 \times 10^{-12}$	$6.71 \pm 0.05 \times 10^{-12}$
Narrow	E (keV)	6.42 ± 0.06	–
Gaussian	σ (keV)	1	–
	EW (eV)	46	44
Broad	E (keV)	$6.05^{+0.82}_{-3.36}$	–
Gaussian	σ (keV)	$3.6^{+3.9}_{-1.1}$	–
	EW (keV)	2.5	2.3
Observed	$F_{2-10keV}$	4.30×10^{-12}	4.65×10^{-12}
flux	$F_{0.5-10keV}$	8.22×10^{-12}	9.52×10^{-12}
Soft-excess	F_{bb}/F_{pl}	0.13 ± 0.01	0.11 ± 0.01
Fit quality	χ^2_ν/dof	1.07/2025	
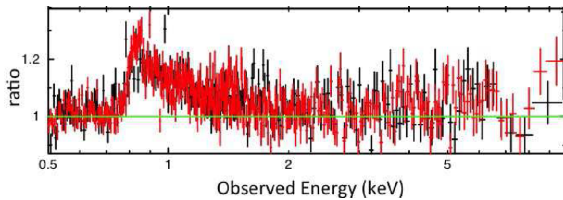
Figure 2. An absorption edge with the same parameter values as those found in Wang et al. (1998) analysis of *ASCA* spectra was added to the model and the residuals (data/model) are shown. These data clearly do not require the absorption edge and allowing the parameters free to vary returned an absorber with negligible optical depth. XMM1 is black, XMM2 is red.

consistent with either process. In the following sections, we examine a physical description for the X-ray emission in HE 0436–4717.

4 UV/X-RAY SPECTRAL ENERGY DISTRIBUTION

X-ray emission provides valuable insight into the accretion process in the inner regions closest to the black hole; however, UV radiation from the accretion disc dominates the bolometric emission. The optical/UV and X-ray bands are investigated together to capture as much of the total accretion emission as possible. One objective in such broad-band analysis is to determine whether or not an AGN is potentially bare.

4.1 The UV-to-X-ray spectral slope

The slope of a hypothetical power law connecting the X-ray (2 keV) and UV (2500 Å) spectral bands (α_{ox}; Tananbaum et al. 1979) was estimated for HE 0436–4717 at both epochs using simultaneous *XMM–Newton* MOS and OM data from the *UVW*1 filter. The UV luminosity at 2500 Å is $\sim 10^{29}\,\mathrm{erg\,s^{-1}}$. The α_{ox} values were

comparable at both epochs with $\alpha_{ox,\,XMM1} = -1.27$ and $\alpha_{ox,\,XMM2} = -1.26$. The higher X-ray flux in XMM2 predicts that the α_{ox} slope be shallower for that epoch – as is the case. These α_{ox} slopes found are reasonable for an AGN of this UV luminosity (Vagnetti, Antonucci & Trevese 2013) and all fall within the span of values calculated by Grupe et al. (2010, hereafter G10) for 92 Type I AGN. The α_{ox} values indicate that HE 0436–4717 is behaving 'normally' (Gallo 2006) and extreme absorption or extreme relativistic effects are not likely to be present.

4.2 Detailed SED modelling using *Swift*

Ideally, one would like to analyse a broad-band SED that can be used in model fitting directly (e.g. Elvis, Lockman & Fassnacht 1994). *Swift* UVOT data from epoch Sw1 were used for the broad-band analysis of HE 0436–4717 as it provides data in five optical bands (as opposed to *XMM–Newton* OM, which observed with only two filters). The XRT Sw1 data provided the 2–10 keVspectrum and the 70-month BAT data were included for the hard X-ray band coverage.

Following the procedures outlined in Vasudevan & Fabian (2009, hereafter VF09) and then expanded upon by Vasudevan et al. (2009, hereafter V09), a basic model composed of a broken power law and a blackbody was applied to the SED. The break radius of the broken power law, R_{br}, is defined as the radius at which the photon index transitions from its inner value, Γ_1, to outer, Γ_2, in units of R_g. Parameters defined in the blackbody accretion disc model included the disc inner radius (R_{in}), the disc normalization (K), and the maximum temperature of the accretion disc (T_{max}). T_{max} was allowed to vary and the inner radius was set to $6R_g$, the innermost stable circular orbit of a Schwarzschild black hole. The normalization is defined as $K = \frac{M_{BH}^2 \cos i}{D_L^2 \, \beta^4}$ where i is the inclination of the disc, D_L the luminosity distance to the source in kpc, and β the spectral hardening ratio. The black hole mass for HE 0436–4717 was adopted from G10 as $M_{BH} = 5.9 \times 10^7\,\mathrm{M_\odot}$ and a luminosity

distance of 233.1 Mpc was used.[3] V09 demonstrated that cos *i* and β could be set to 1 for type-I AGN, and thus the value for *K* was calculated and fixed in the initial fits.

The assumption regarding β is reasonable due to the nature of the analysis and the DISKPN model: β is the $T_{color}/T_{effective}$ ratio that is designed to correct flux in the far-UV band of a spectrum in order to preserve the total integrated bolometric luminosity (Shimura & Takahara 1995). In the model DISKPN, a decrease in β will boost flux across all wavebands, not just in the far-UV. In addition, as only near-UV data were used in the SED fitting, no colour correction is ultimately required. As for inclination or cos *i*, its influence on the overall normalization is minimal compared to both M_{BH} and D_L, which are both raised to the second power. In general, a change in the normalization parameter, *K*, *overall* does not alter the spectral shape of the component significantly, but rather adjusts the peak temperature of the (estimated) blackbody in order to better fit the data.

Assuming a Comptonization origin for the primary X-rays, the low-energy break in the power law corresponded to T_{max} of the disc component; $R_{br} = 4\,T_{max}$ specifically (VF09). Galactic absorption was set to $N_H = 1.03 \times 10^{20}\,cm^{-2}$ and intrinsic extinction was considered in various ways, as will be described below. Optical filters (*V*, *B*, and *U*) were not used for fitting as host galaxy contamination was not accounted for; the optical data were plotted simply for comparison. The XRT data were also fit over a reduced range of 2–10 keV. This limit was placed to ensure the primary X-ray emission was fit rather than the SE which may originate from a different component. The BAT data were not fit at all and were simply overplotted for visual comparison.

The first model tested (Model A) described the simplest case where only Galactic extinction modified the intrinsic broad-band spectrum. This scenario did not describe the data well ($\chi^2 = 102/30$ dof), overestimating the UV spectral slope significantly. Galactic extinction alone cannot explain these data. Host galaxy extinction was then added to the model and allowed to vary (Model B). The fit improved by $\Delta\chi^2 = 71$ for an additional free parameter. The extinction that described the SED best was $E(B–V) = 0.095 \pm 0.011$. This scenario describes the broad-band spectra very well; however, it seems contradictory with the X-ray analysis performed previously. Assuming the estimated extinction, the corresponding column density can be calculated using the relationship outlined by Predehl & Schmidt (1995): $N_H = 5.3 \times 10^{21}\,cm^{-2}\,E(B–V)$. For $E(B–V)$ ranging from 0.084 to 0.105, $N_H = (5.04 \pm 0.58) \times 10^{20}\,cm^{-2}$, which is at least 50 times the upper limit measured from the X-ray spectra (see Section 3). Moreover, G10 measures extinction from the Balmer decrement and finds $E(B–V) = 0.04$, which is much lower than the intrinsic extinction estimated in Model B.

Next, the intrinsic extinction measured from the Balmer decrement was adopted and the *K* was allowed to vary (Model C). The best value was $K = (52.16 \pm 14.30) \times 10^{-4}\,M_\odot^2\,kpc^{-2}$ and $L_{0.001-100\,keV} = 6.47 \times 10^{44}\,erg\,s^{-1}$, giving an Eddington luminosity ratio of $L_{Bol}/L_{Edd} = 0.09$. Model C provides a better fit than Models A and B, and the treatment of the extinction is physically motivated by the measured Balmer decrement.

The final possibility tested is that the SED can be entirely described by allowing only the disc normalization to vary with only Galactic extinction (Model D). The fit statistic was the comparable

to Model C and $K = (107.54 \pm 25.77) \times 10^4\,M_\odot^2\,kpc^{-2}$. In this case, $L_{0.001-100\,keV} = 4.99 \times 10^{44}\,erg\,s^{-1}$ and so $L_{Bol}/L_{Edd} = 0.07$.

A summary of the model variations with their respective parameters and Eddington ratios are listed in Table 3. Excluding the SE in this analysis has negligible impact as in the most extreme case (i.e. lowest luminosity) it contributes less than 4 per cent to the bolometric luminosity. The SED models with high extinction values seem at odds with the initial X-ray analysis, extinction measured from the Balmer decrement (G10), and the UV spectral analysis of Halpern & Marshall (1996). Alternatively, the SED can also be explained if we assume the source is not substantially reddened, but that the ratio $(M_{BH}/D_L)^2$ is uncertain by a factor of 6–10. This is perhaps not unreasonable. The black hole mass for HE 0436–4717 was not from reverberation mapping, but rather based on a single-epoch mass estimate which could be uncertain by a factor of a few (Vestergaard & Peterson 2006).

The *Swift* BAT data were included for visual inspection of the high-energy trend; however, the BAT data were not fitted. Although the uncertainty in the BAT data allow for a wide spread, the extrapolated models were all consistent with these data. Model C (i.e. Balmer decrement based intrinsic extinction and *K* allowed to vary) is shown for both the observer and source frame (see Fig. 3).

The Eddington ratios determined from the *Swift* SED analysis agree with the value of 0.08 found by G10 for this object. An Eddington ratio around 0.08 is not unusual, although it does fall on the lower end of the probability distribution described by V09 in their analysis of 26 low-*z* AGN (see V09 fig. 15, left-hand panel). A lower Eddington ratio implies HE 0436–4717 is not a rapid accreter.

5 DETAILED X-RAY SPECTRAL ANALYSIS

The first glance at the broad-band X-ray spectra of HE 0436–4717 showed the presence of multiple components and the nature of the excess residuals above ~6 keV remains unclear. Three scenarios are considered to describe the X-ray spectra of HE 0436–4717 in a self-consistent manner: partial covering absorption, blurred reflection, and soft Comptonization.

5.1 Partial covering absorption

Turner & Miller (2009) explain in detail how gas with a range of column densities can influence the primary component of an AGN. As absorbers move in the field of view, some of the intrinsic radiation is both scattered and absorbed. Both changes in the covering fraction and column density can create spectral variability over a range of time-scales. A strong SE can appear at lower energies and even the Fe Kα line can be broadened by absorption with the red shoulder being enhanced by attenuation rather than by relativistic effects. A thorough attempt was made to fit the X-ray spectrum of HE 0436–4717 with absorption in an effort to determine the origin of the X-ray emission in this object.

The model ZPCFABS was used to begin testing for possible neutral absorption signatures. A single, neutral absorber was applied to a simple power law and fit to both epochs of the merged MOS data. Scenarios were tested in which only the covering fraction remained free to vary between the epochs (i.e. variability attributed to absorbers) and also having only the primary component vary instead (i.e. variability attributed to primary emitter). The overall goodness of fit remained poor in both cases. Double neutral absorption was an improvement, though the model continued to underestimate the data at higher energies. This scenario called for the two absorbers

Table 3. The four models used to fit the UV-to-X-ray SED. Column 1 lists the model parameters and goodness of fit. Column 2 shows the parameter values for each model. Parameters that are fixed are listed without errors.

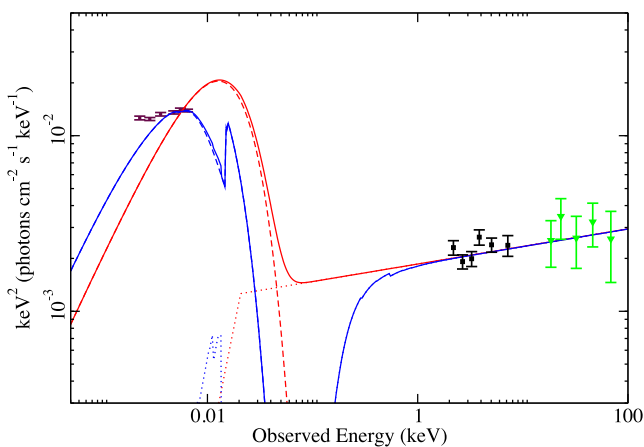| (1)	(2)			
	SED models			
Parameters	A	B	C	D
$L_{0.001-100\,\mathrm{keV}}$ ($\times 10^{44}$ erg s^{-1})	6.39	15.17	6.47	4.99
$E(B-V)_{\mathrm{int}}$	0	0.095 ± 0.011	0.04	0
$E(B-V)_{\mathrm{Gal}}$	0.009	0.009	0.009	0.009
T_{max} (eV)	5.26 ± 0.01	6.85 ± 0.21	3.11 ± 0.25	2.35 ± 0.14
K ($\times 10^4\,\mathrm{M_\odot}^2\,\mathrm{kpc}^{-2}$)	6.41	6.41	52.87 ± 14.30	107.54 ± 25.77
Power-law norm. ($\times 10^{-2}$) (ph keV^{-1} cm^{-2} s^{-1})	1.36 ± 0.06	0.63 ± 0.06	6.22 ± 1.42	14.16 ± 2.59
$L_{\mathrm{Bol}}/L_{\mathrm{Edd}}$	0.08	0.20	0.09	0.07
χ_ν^2/dof	3.50/30	1.06/29	1.03/29	1.02/29

Figure 3. An SED comparison of Model C with intrinsic extinction determined by the Balmer decrement and the disc parameter K allowed to vary. The solid lines represent the total model in the source (red) and observed (blue) reference frames. The dashed line represents the disc component while dotted shows the primary X-ray component. Only the XRT data (black squares) from 2.0–10.0 keV and the UV data of the UVOT (tiny maroon circles) were fitted, the 70-month *Swift* BAT data (green triangles) were overplotted for visual inspection. Only the XRT data that were fit (i.e. between 2–10 keV) were included for clarity.

to have very different densities (see Table 4) and could potentially describe a single absorber with a density gradient along the line of sight, rather than two completely independent bodies. The column densities remain consistent in the two epochs and so would not alone explain any spectral variability seen over longer time-scales. Allowing only the primary emitter to vary instead did not improve the fit quality significantly. Apparently, if there is any variability in the primary emitter on long time-scales, it is subtle.

5.2 Ionized partial covering

Next, a fit with a single ionized absorber was attempted. The ionized absorber was modelled by ZXIPCF. Once again, all parameters except for covering fraction were linked at the epochs in an effort to describe the long-term variability with changes in an absorber. There were residuals to the model and the fit quality was poor (χ^2/dof = 2415/2032). The covering fraction was not significantly different from one epoch to the next.

If the photon index of the primary component is allowed to vary while the absorber is frozen and linked across the epochs, the fit improves by $\Delta\chi^2 = 213$ for two additional free parameters, however some positive residual features remain. The photon index in XMM2 increases, going from $\Gamma = 2.16 \pm 0.01$ to $\Gamma = 2.24 \pm 0.01$, consistent with the trend found in the toy model fits. It appears that the model with a single ionized absorber detects a slight, long-term variability from the primary emitter while the model with a single neutral absorber does not.

A second ionized absorber was added to the model and the parameters reset so that only the covering fractions were unlinked across the epochs. The fit was significantly better than that of the single absorber (χ^2/dof = 2150/2028) and no residual features remained (see Fig. 4), although the covering fractions for both absorbing bodies remained similar at both epochs (see Table 4). Thus, as a final exercise, one absorber was kept constant throughout the epochs while the other was allowed to vary in N_{H} and ξ, with Γ free to vary as well. The goodness of fit remained unchanged and the parameters that were allowed to be independent in XMM2 did not significantly change from their XMM1 values.

None of the ionized absorption model variations defined the source of long-term variability uniquely; however, the scenario in which only the covering fraction varied between epochs did result in the best goodness of fit. The most satisfying absorption model overall describes two ionized absorbers, the first more ionized and with a higher column density than the second, with both having comparable covering fractions. Both absorbers are found to have redshifts comparable to the source that remained steady across the epochs.

The ionized partial covering model was extrapolated to higher energies and visually compared to the *Swift* BAT data. Model residuals show that, despite the partial covering scenario's ability to describe the 0.5–10 keV spectra well, it underpredicts the X-ray flux above 10 keV (Fig. 4, residuals). However, photoelectric absorption will also produce its own reprocessed emission in addition to the intrinsic radiation it attenuates (e.g. Turner & Miller 2009). Reprocessed emission from absorption would affect both the hard X-ray flux and flux of the Fe Kα line.

Following Reynolds et al. (2004), we estimate the strength of an Fe Kα emission line that would be produced from the denser of the two absorbers in the partial covering model. Assuming the number of ionizing photons between 7 and 20 keV that are re-emitted in the neutral iron line at 6.4 keV is governed by the fluorescent yield of neutral iron (0.347), we estimate the flux in the iron line

Table 4. The best spectral absorption models in the 0.5–10.0 keV band. Models are listed in column 1 and their components in column 2. Model parameters are in column 3 and their values in columns 4 and 5 for XMM1 and XMM2, respectively. Parameters linked across the epochs are denoted by dots.

(1) Model	(2) Model component	(3) Model parameter	(4) XMM1	(5) XMM2
Double neutral absorption	Absorber 1	N_H (cm^{-2})	$26.30^{+3.27}_{-2.94} \times 10^{22}$	...
		CF	0.61 ± 0.02	0.56 ± 0.02
	Absorber 2	N_H (cm^{-2})	$1.33^{+0.10}_{-0.09} \times 10^{22}$	...
		CF	0.48 ± 0.02	0.42 ± 0.02
	Primary flux	Γ	2.66 ± 0.03	...
	fit quality	χ^2_ν/dof	1.11/2030	
Double ionized absorption	Absorber 1	N_H (cm^{-2})	$44.62^{+5.46}_{-6.27} \times 10^{22}$	...
		$\log(\xi)$ [erg cm s^{-1}]	$1.59^{+0.34}_{-0.30}$	...
		CF	$0.67^{+0.02}_{-0.03}$	0.63 ± 0.03
	Absorber 2	N_H (cm^{-2})	$1.75^{+0.14}_{-0.13} \times 10^{22}$	...
		$\log(\xi)$ [erg cm s^{-1}]	$0.48^{+0.13}_{-0.10}$	...
		CF	0.52 ± 0.03	0.44 ± 0.04
	Primary flux	Γ	2.63 ± 0.05	...
	Fit quality	χ^2_ν/dof	1.06/2028	

should be approximately 2.70×10^{-13} erg cm^{-2} s^{-1} for XMM1, 2.55×10^{-13} erg cm^{-2} s^{-1} for XMM2. Such a narrow line would have an equivalent width of EW ≈ 210 eV and 200 eV, in the spectrum of XMM1 and XMM2, respectively. The strength of the narrow Fe Kα emission line in the spectra of HE 0436–4717 is only about 40 eV, much weaker than expected if arising from reprocessing, but we note that various effect such as Compton-thick lines-of-sight could generated weaker lines than predicted (e.g. Yaqoob et al. 2010).

Finally, an unblurred reflection component REFLIONX (Ross & Fabian 2005) was added to the absorption model to model for any narrow Fe Kα emission, but also to adjust the residuals above 10 keV seen in Fig. 4. The modification above 10 keV was negligible, which

Figure 4. The ionized partial covering model (Table 4) and its relation to the MOS spectra. A pair of ionized absorbers were fit from 0.5–10.0 keV with the covering fraction as the only parameter varying at both epochs. The XMM1 (black) and XMM2 (red) data are shown with the constant intrinsic power law determined by the model (dotted blue) in the top panel. The model was extrapolated above 10 keV for visual comparison with 70-month *Swift* BAT data (yellow) and the corresponding residuals are shown (bottom panel).

is expected given the steep photon index required to fit the spectra below 10 keV.

5.3 Blurred reflection

The multi-epoch observations of HE 0436–4717 were next fitted with a blurred reflection model. The primary X-ray source was modelled as a cutoff power law with the high-energy cutoff fixed at 300 keV. The backscattered emission from the accretion disc, modelled with REFLIONX, was modified by relativistic effects close to the black hole (Fabian et al. 1989). We adopted KDBLUR2 for the blurring kernel, which incorporates a twice broken power law for the emissivity profile.

The disc inclination (i), iron abundance (A_{Fe}), and inner disc radius (R_{in}) are not expected to change over the observable time-scales and were linked between epochs. The iron abundance was initially fixed to solar, the outer disc emissivity profile (q_{out}) was fixed to 3, and the break radius (R_b) where the emissivity index changes from q_{in} to q_{out} was fixed to $R_b = 6 \, R_g = 6 \, \frac{GM}{c^2}$. At each epoch, the ionization parameter ($\xi = 4\pi F/n$, where n is the hydrogen number density and F is the incident flux), normalization of the reflector, the incident power-law photon index, and normalization were all free parameters.

The measurement of iron abundance is rather sensitive and degeneracies have been found with other fit parameters like emissivity, inclination, and black hole spin (or comparably, the inner disc radius). Contour plots were generated between various fit parameters to determine if the low iron abundance could be an artefact of the modelling, but in all cases the iron abundance remained consistently low (Fig. 5).

A second REFLIONX component that was not blurred and whose flux remains linked between epochs was also included to mimic emission from a distant reflector like the torus. The ionization parameter of this distant reflector was fixed at $\xi = 1$ erg cm s^{-1} and the iron abundance set to the solar value. The photon index of the power law source illuminating the torus is fixed at $\Gamma = 1.9$, the canonical value for AGN (e.g. Nandra & Pounds 1994). There is
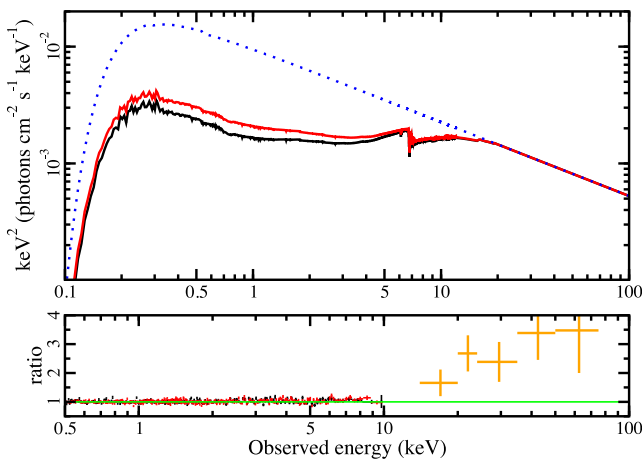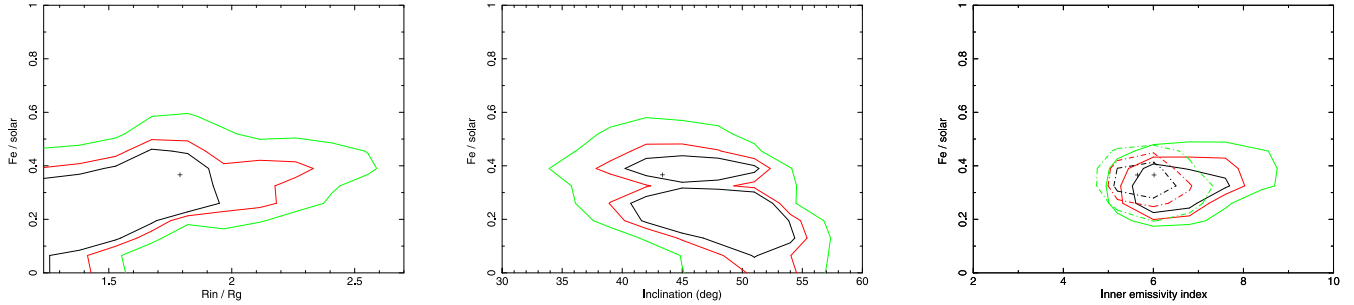
Figure 5. Contours are calculated to examine the dependence of the measured iron abundance with various other parameters. The iron abundance is compared to the inner disc radius (left), disc inclination (centre), and inner emissivity profile (right). In the right-hand panel the solid and dashed contours are for data set 1 and 2, respectively. The contours correspond to a 2.3, 4.61, and 9.21 delta fit statistic.
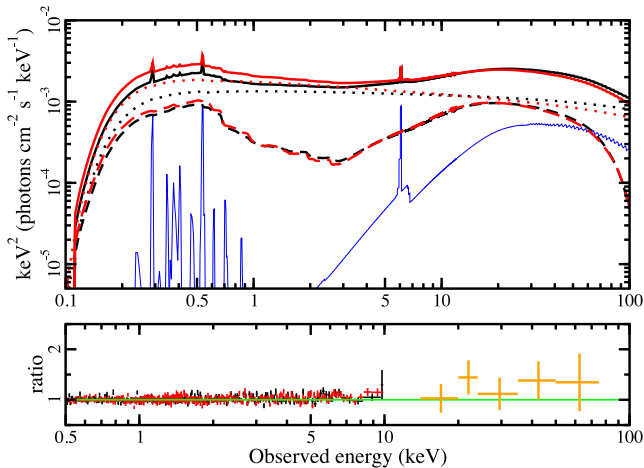

Figure 6. The blurred reflection model for the two epochs (top panel). The primary X-ray component is dotted while the blurred reflector is dashed. The distant reflector (same in both epochs) is solid blue. The total summed model is solid black and red, for XMM1 and XMM2, respectively. The model was extrapolated above 10 keV for visual inspection with the BAT data (yellow) and the residuals (model/data) are shown (bottom panel).

no reason to assume that the radiation incident on the distant reflector will be the same as that from the primary component and if a value of $\Gamma = 2.0$ is used instead it does not significantly alter the fit statistic.

The described model produced a reasonable fit to both spectra ($\chi_\nu^2/\mathrm{dof}=1.08/2025$), but left excess residuals above 5 keV. Permitting q_{out} and R_b to vary at each epoch did not substantially improve the fits, but a significant improvement ($\Delta\chi^2 = 33$ for 1 additional fit parameter) was found if the iron abundance was allowed to vary. The resulting fit was good ($\chi_\nu^2/\mathrm{dof} = 1.06/2024$; Fig. 6, Table 5), but noteworthy was the low, sub-solar iron abundance measurement ($A_{\mathrm{Fe}} = 0.36^{+0.04}_{-0.16}$).

Further examination to determine if the low iron abundance was a result of the fit procedure were carried out. The iron abundance of the distant reflector was linked with the inner, blurred reflector to determine if enhancing the iron 'signal' could result in a more typical measurement. This fit was an improvement over the initial fit, with the abundance fixed at solar ($\Delta\chi^2 = 25$ for 1 additional fit parameter), but the resulting measurement was comparable to the measurement from the blurred component alone ($A_{\mathrm{Fe}} = 0.33^{+0.14}_{-0.17}$).

Strong degeneracy has been noted between the black hole spin parameter (a) and the iron abundance (e.g. Reynolds 2013). The weak reflection features and moderate signal to noise of the data

do not justify a thorough examination into black hole spin. However, the possibility that the low iron abundance may be rectified with treatment of the black hole spin should be considered. With this in mind, the blurring kernel KDBLUR2 was replaced with RELCONV (Dauser et al. 2010) which includes (retrograde and prograde) black hole spin as a measured parameter. The fit quality was comparable to that achieved with KDBLUR2 ($\chi_\nu^2/\mathrm{dof} = 1.06/2024$). The spin parameter was high ($a \approx 0.96$) and was consistent with the value of the inner disc radius reported in Table 5. The iron abundance continued to remain low ($A_{\mathrm{Fe}} \approx 0.28$). Forcing the model to accommodate a retrograde spin ($-0.998 \le a \le 0$) only resulted in a poorer fit ($\chi_\nu^2/\mathrm{dof} = 1.11/2024$) and did little to enhance the iron abundance ($A_{\mathrm{Fe}} \approx 0.56$).

Further consideration was to adopt a different reflection code. The reflection model REFLIONX was replaced with XILLVER (García et al. 2013). There are several differences between XILLVER and REFLIONX including XILLVER's ability to calculate reflected intensity for each photon energy, position, and viewing angle whereas REFLIONX uses an angle-average integration for reflected intensity. Primarily, we consider if these differences could be attributed to the low iron abundance in HE 0436–4717. Substituting REFLIONX for XILLVER in the original model (Table 5) resulted in an equally good fit ($\chi_\nu^2/\mathrm{dof}= 1.07/2024$) with comparable parameters measurements. We note the iron abundance boundary value in XILLVER is 0.5, which makes it impossible to explore values as low as we found with REFLIONX. None the less, the best-fitting iron abundance pegs at the lower limit of the model ($A_{\mathrm{Fe}} = 0.50^{+0.23}_{-0}$).

5.4 Soft Comptonization

Both the absorption and reflection scenarios addressed in the previous sections fit the SE of HE 0436–4717 well and it is statistically impossible to distinguish between the two scenarios without further analysis. A third possibility is that the SE could be emerging from a second Comptonizing region.

Observations of binary black holes have shown that spectral fitting can require two Comptonizing regions (Kubota & Done 2004; Done et al. 2012, hereafter D12). While there are several possibilities for the source of the second softer Compton up-scattered photons, D12 assume such soft Comptonization is originating from the accretion disc itself. The authors postulate that disc structures could deviate from the standard Shakura–Sunyaev model at inner radii, as has been proposed for some of the more extreme Seyfert galaxies like narrow-line Seyfert 1s . In particular, they consider enhanced dissipation of disc outer layers that would create a Compton up-scattered flux in the soft X-ray band.

Table 5. The best-fitting blurred reflection model fit simultaneously to the *XMM–Newton* merged MOS spectra. The model components and model parameters are listed in columns 1, and 2, respectively. Columns 3 and 4 list the parameter values during the XMM1 epoch and XMM2 epoch, respectively. Parameters that are fixed are listed without errors and the dots denote those that are linked across the epochs. The reflection fraction ($\mathcal{R}$) is approximated as the ratio of the reflected flux over the power law flux in the 0.1–100 keV band. Fluxes are corrected for Galactic absorption and are reported in units of $\mathrm{erg\,cm^{-2}\,s^{-1}}$.

(1) Model component	(2) Model parameter	(3) XMM1	(4) XMM2
Incident	Γ	2.03 ± 0.02	$2.14^{+0.03}_{-0.07}$
Continuum	E_{cut} (keV)	300	–
	$F_{0.1-100\,keV}$	$1.35 \pm 0.06 \times 10^{-11}$	$1.66 \pm 0.08 \times 10^{-11}$
Blurring	q_{in}	$6.0^{+2.0}_{-0.7}$	5.6 ± 0.7
	R_{in} (R_g)	<1.80	–
	R_{out} (R_g)	400	–
	R_b (R_g)	6	–
	q_{out}	3	–
	i (°)	45^{+8}_{-7}	–
Reflection	ξ ($\mathrm{erg\,cm\,s^{-1}}$)	150^{+320}_{-48}	56^{+41}_{-11}
	A_{Fe} (solar)	$0.36^{+0.04}_{-0.16}$	–
	$F_{0.1-100\,keV}$	$4.90 \pm 0.63 \times 10^{-12}$	$4.79 \pm 0.52 \times 10^{-12}$
	$\mathcal{R}$	0.36 ± 0.05	0.29 ± 0.03
Distant reflector	ξ ($\mathrm{erg\,cm\,s^{-1}}$)	1.0	–
	A_{Fe} (solar)	1.0	–
	Γ	1.9	–
	$F_{0.1-100\,keV}$	$1.62^{+0.52}_{-0.20} \times 10^{-12}$	–
Fit quality	χ^2_ν/dof	1.06/2024	

As an initial investigation into a double-Comptonization scenario, the merged MOS spectra were fit from 0.5–10.0 keV with a basic power law + Comptonization model with the second Comptonization component provided by COMPTT (Titarchuk 1994). The seed photons were assumed to be supplied by the intrinsic UV disc radiation below the observed bandpass and both the seed photon temperature and the temperature of the second Comptonizing region were allowed to vary. This lone double-Comptonization model did not fit well (χ^2/dof = 2319/2030) and there were clear residuals around 6.4 keV. When a distant reflector was added, the fit improved by $\Delta \chi^2 = 99$ for two additional free parameters, but the new model did not account for all of the iron line flux. If a broad line was added in the form of blurred reflection, the spectra were well modelled in the 5–8 keV range, however the normalization of the second Compton component dropped by an order of magnitude and the optical depth reduced from around 2 keV to $\tau \sim 0.09$ as blurred reflection now accounted for the soft band. A simple double-Comptonization scenario appears to model the SE appropriately, but does not fit some of the curvature between 0.5 and 10.0 keV (Fig. 7).

In an attempt to model the full 0.5–10.0 keV spectra more physically, the data were fitted with OPTXAGNF (D12). Black hole mass and luminosity distance were frozen at their known values of $5.9 \times 10^7 \, M_\odot$ and 233.1 Mpc, respectively. The Eddington fraction was set at $\log(L/L_{Edd}) = -1.05$ as determined by the SED fitting, a value that – as mentioned previously – agrees with the fraction found by G10. Black hole spin was set to $a = 0.5$ to start and the normalization was fixed at unity as per model instructions.[4] For the initial fitting, only the power-law parameters were allowed to vary independently across the epochs and all other parameters were frozen.
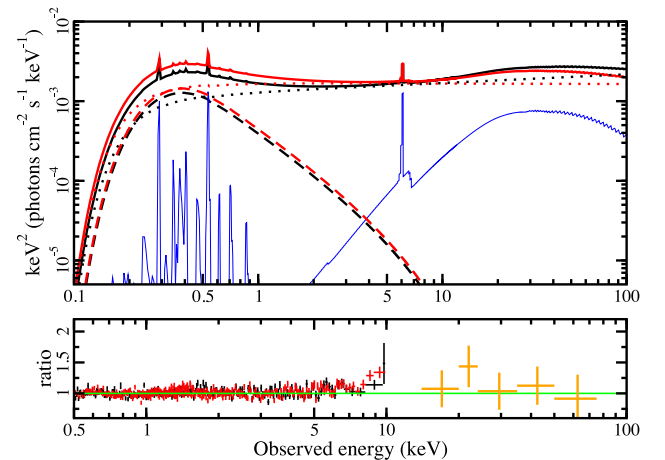
Figure 7. The double-Comptonization model for the two epochs (top panel). The primary X-ray component is dotted while the second Compton component is dashed. The distant reflector (same in both epochs) is solid blue. The total summed model is solid black and red, for XMM1 and XMM2, respectively. The model was extrapolated above 10 keV for visual inspection with the BAT data (yellow) and the residuals (model/data) are shown (bottom panel).

Parameters were systematically thawed and unlinked to gradually increase complexity as needed to improve the fit. The parameters f_{pl}, R_{cor}, kT_e, and τ_e remained consistent between the epochs when allowed to vary and so were kept linked. Although it is reasonable to allow these components to vary between epochs, they did not improve the quality of the fit if unlinked and so, after an initial test of allowing them free to vary at both epochs, they were re-linked.

The initial fit was very poor (χ^2/dof = 2475/2032) with a clear iron line residual and other residual features at about $E \leq 1$ keV. The

Table 6. Summary for the best soft Comptonization model. All parameters are frozen with the exception of: R_{cor}, kT_e, τ, Γ, f_{pl} and all parameters are linked across the epochs with the exception of Γ.

(1) Component	(2) Parameters	(3) XMM1	(4) XMM2
Distant reflection	A_{Fe} (solar)	1.0	–
	Γ_{dr}	1.0	–
	ξ (erg cm s^{-1})	1.0	–
	z	0.053	–
	norm$_{dr}$	$(1.56 \pm 0.35) \times 10^{-5}$	–
Absorption edge	E_{edge} (keV)	$0.77^{+0.03}_{-0.02}$	–
	$\tau_{max, edge}$	$(9.13 \pm 0.02) \times 10^{-2}$	–
Soft Comptonization	M_{BH} (M$_\odot$)	5.9×10^7	–
	D_L (Mpc)	233.1	–
	$\log(L/L_{Edd})$	-1.05	–
	$\log R_{out}$	3	–
	a	0.8	–
	R_{cor} (R_g)	$11.55^{+5.41}_{-1.50}$	–
	kT_e (keV)	$0.61^{+0.20}_{-0.11}$	–
	τ	$7.73^{+1.19}_{-1.27}$	–
	Γ	$1.80^{+0.01}_{-0.02}$	$1.98^{+0.03}_{-0.05}$
	f_{pl}	0.44 ± 0.01	–
χ^2_ν/dof		1.09/2029	

fit proved difficult to constrain when the spin parameter was allowed to vary freely, so the fit quality was instead tested at different fixed values of a. A zero spin only worsened the fit ($\Delta\chi^2 = 148$), while testing a maximum spin value of $a = 0.998$ improved the fit by $\Delta\chi^2 = 303$ for no additional free parameters. Fixing the spin at a moderately high value of $a = 0.8$ improved the goodness of fit even further, with $\Delta\chi^2 = 12$ for the same number of free parameters, and a was kept frozen at this value. If the Eddington ratio is allowed to vary with spin, neither parameter changes significantly from their best-fitting values and the fit statistic remains comparable.

To improve the fit, a distant reflector was added in the same manner as Section 5.3. The distant reflector improved the fit significantly, $\Delta\chi^2 = 101$ for one additional free parameter, and the iron line residuals were resolved. Curiously, the data remained overestimated around 0.8 keV until an absorption edge was included at the redshift of the source, with both its energy and optical depth free to vary. The absorption feature was found to have an energy of $E \sim 0.77$ keV and $\tau \sim 0.09$ – consistent with O VII, though the accompanying O VIII absorption edge was not detected. We noted this is the only model that shows marked improvement with the addition of an absorption edge. The addition of both a distant reflector and an absorption edge provided the best description of the data in the soft Comptonization scenario (χ^2/dof = 2211/2029) and the model that most satisfies the data is summarized in Table 6.

The model was extrapolated into the 10–100 keV band and the BAT data was overplotted for comparison. The model components (top panel) and residuals that include the BAT data (bottom panel) are shown in Fig. 8. The BAT data were only over plotted for comparison and were not included in the fit. The model slightly underestimates the fluxes seen above 10 keV.

Unlike the partial covering or blurred reflection models, the OPTXAGNF model provides some information regarding the UV, disc dominated emission. Thus, it is advantageous to explore if the best soft Comptonization model is consistent with the *Swift* UVOT data. Simply extrapolating the model to the UV band shows a poor fit
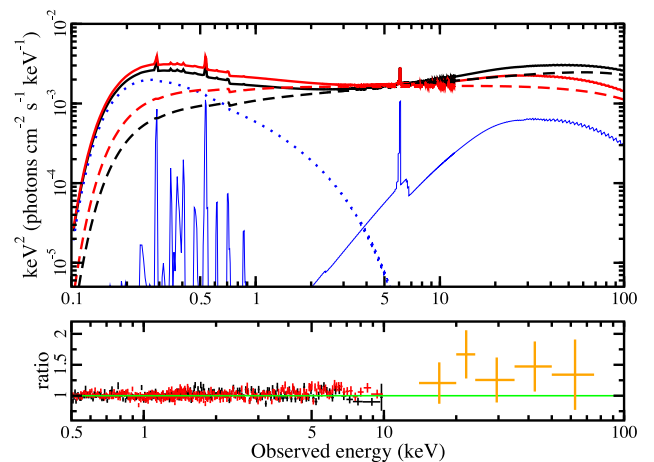

Figure 8. The soft Comptonization model (Table 6) is shown in the top panel. XMM1 is black and XMM2 is red. The hard power-law component is shown as the dashed line. The soft Comptonization component that is common at both epochs is shown as a dotted blue curve. The distant reflect, also common at both epochs, is shown as the fine, solid, blue curve. The model was extrapolated >10 keV for comparison with the BAT data (yellow) and the corresponding residuals (data/model) are shown (bottom panel).

using the assumed black hole mass and luminosity distance, as did our initial SED fits (Section 4.2). Allow the black hole mass and distance to vary does not significantly improve the fit since the statistics are driven by the X-ray data, but it does suggest there could be a discrepancy of at least 2 in the M_{BH}/D_L ratio comparable with our finding with the SED modelling.

In an further attempt to fit the UV data, the parameters defining the disc component – black hole mass, Eddington ratio, and spin – were all allowed to vary. The fit is comparable to that of the X-ray only data (χ^2/dof = 2246/2029); however, the model underestimated the UV flux. The black hole mass increased by $\sim$27 per cent
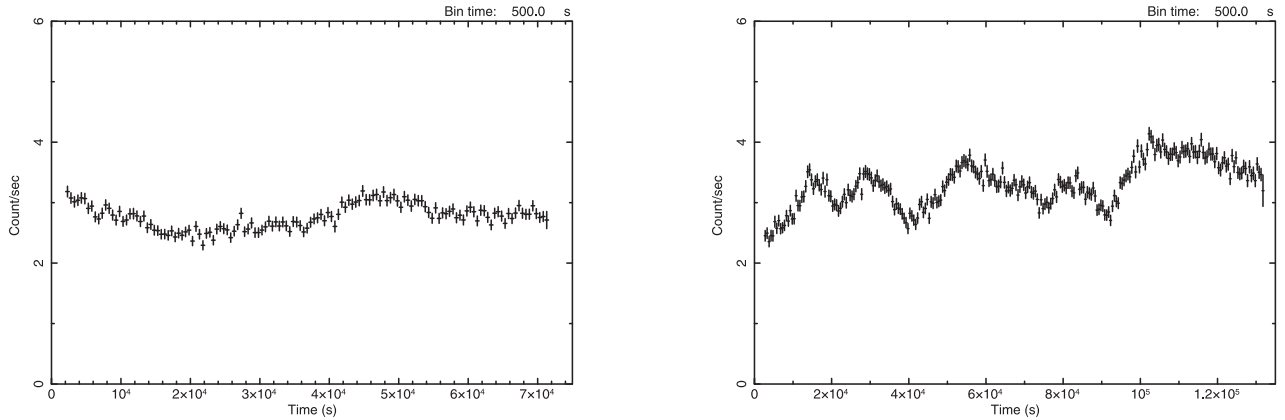
Figure 9. MOS light curves for both XMM1 (left) and XMM2 (right) binned at 500 s each. XMM2 had nearly double the duration (note *x*-axes) and also displays more variability. Zero marks the start of each exposure.

while spin decreased by ∼ 20 per cent; the Eddington ratio remained unchanged. If the remaining parameters – those that describe the X-ray components and the absorption edge – are free, the fit statistic does not change significantly and neither do the parameter values. Lastly, an absorber was added to the model to mimic intrinsic extinction in the UV. This broad-band soft Comptonization model with absorption fits well (χ^2 /dof = 2213/2028); however, it predicted an intrinsic extinction of $E_{B-V, \text{int}} = 0.055$ which requires a column density of $N_\text{H} = 2.99 \times 10^{20}\,\text{cm}^{-2}$: 29 times higher than that predicted by the X-ray data ($N_\text{H} < 10^{19}\,\text{cm}^{-2}$). Once again it appears that an absorption scenario is statistically acceptable for HE 0436–4717, albeit inconsistent with further scrutiny.

6 TIMING ANALYSIS

Source photons were extracted to create light curves in a variety of energy bands between 0.2 and 12.0 keV, including a broad-band 0.2–12.0 keV bin. The light curves from all EPIC instruments that collected data proved consistent in the XMM1 and XMM2. All subsequent timing analyses utilized MOS data only. MOS 1 and 2 light curves were combined at each epoch, taking care to match the observation start and stop times. The 0.2–12.0 keV merged MOS light curve for each epoch is shown in Fig. 9.

6.1 Hardness ratios

Ratios of softer energy band count rates over those of a harder energy band were calculated for four energy band pairs between 0.2 and 12.0 keV range. Bins were selected such that there were a comparable number of counts in each band. These HR were analysed two ways at each epoch: flux-dependent HR; and as time-dependent, normalized HR.

The hardness as a function of count rate did not reveal any significant correlation at either epoch. This does not mean the spectra are not variable, but only that any variability is not significantly dependent on the specific flux state. The hardness as a function of time was similar: within the calculated uncertainties it appears there is little time-dependent variation in the soft bands over time. All HR trends for the X-ray data were nearly linear within uncertainties and so indicate little to no change in HR with respect to either flux or time. This does not mean that the spectral components are not variable, but rather that any variability that may be present occurs in such a way as to maintain a constant flux ratio between energy bins.

A more thorough analysis is needed to further probe the temporal behaviour in HE 0436–4717 and this is explained in the following sections.

6.2 Fractional variability

The fractional variability amplitude (Edelson et al. 2002), F_var, is a useful measurement used to quantify the intrinsic variability of a light curve while also accounting for uncertainty. This parameter compares the amplitude of any variations present in each energy band to determine if the amplitudes in one energy band are larger than those in another. The F_var thus compares the relative 'strengths' of observed variability across two energy bands, independent of time or flux. The F_var is defined as

$$F_\text{var} = \frac{1}{\langle X \rangle} \sqrt{S^2 - \langle \sigma_\text{err}^2 \rangle}, \tag{1}$$

where $\langle X \rangle$ is the mean count rate, S^2 the total variance of the light curve, and $\langle \sigma_\text{err}^2 \rangle$ the mean error squared. Uncertainties were determined following the procedure of Ponti et al. (2004).

The F_var was calculated for both epochs using merged MOS light curves. The light curves were binned at 1000 s and a total of nine energy bins were used spanning 0.2–10.0 keV; data above 10 keV were ignored due to the low signal to noise. XMM2 displays a higher F_var than XMM1 overall, which is apparent in the light curves (e.g. Fig. 9).

In terms of the blurred reflection model, variations in the primary component (i.e. power law) may solely account for the shape of the F_var spectrum. From the blurred reflection model found previously, the fraction that the power law contributes to each energy band was determined and overplotted on the F_var spectrum for both epochs (Fig. 10, dashed blue line). In the blurred reflection model, it seems reasonable to attribute most of the rapid variability to changes in the power-law normalization, specifically. In this very simplified scenario, the reflection model prediction disagrees with the data in a few bins (around 0.4 keV and between 1 and 2 keV, for example). The best that can be said is that the overall model trend does agree with the linear shape of the fractional variability spectrum.

When the process is repeated for the partial covering absorption model, the predicted F_var profile is less constrained (Fig. 10, dotted green line). Testing the partial covering scenario is more challenging as the source of variability could be the absorber as well as the primary component. The same difficulty lies in modelling soft
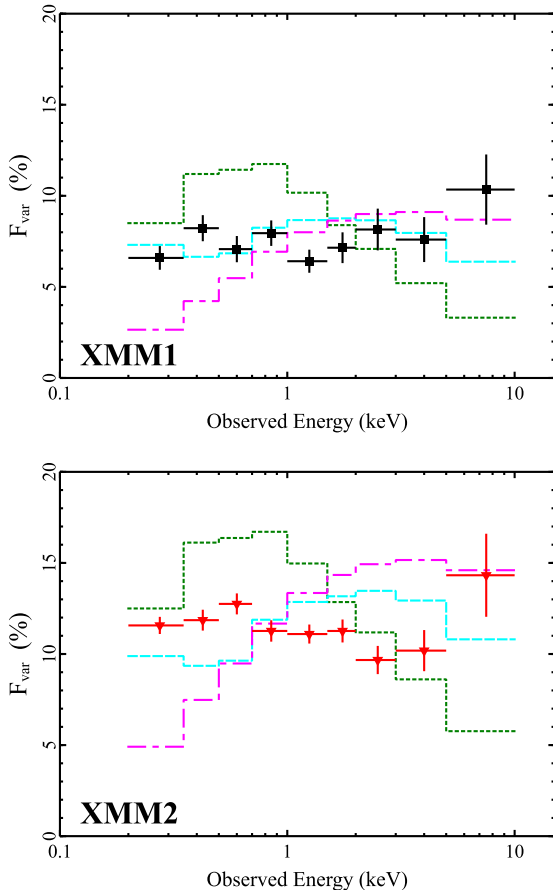
Figure 10. Fractional variability analysis with spectral model predictions. The fraction that the power law contributes to each energy band is overplotted on the F_{var} spectrum for both XMM1 (top panel) and XMM2 (bottom panel). The reflection (blue dashed line), absorption (green dotted line), and double-Comptonization (magenta dot–dashed line) model predictions are compared for each epoch.

Comptonization: there could be many sources of variability. For completeness, a profile was created using the double-Comptonization model of Section 5.4, with the hard Compton component assumed to be the sole source of variability (Fig. 10, dot–dashed magenta line).

Looking at the three model predictions for both epochs, it is clear that there must be more to the story. Perhaps only a fraction of the total power-law flux is varying or perhaps an additional component contributes to the total variability. The F_{var} analysis indicates that multiple parameters need to vary if any model is to describe the spectral data.

6.3 Flux-resolved spectra

Flux-resolved spectra were made in an effort to resolve the mechanism(s) behind short-term variability in HE 0436−4717. As XMM2 was considerably longer and shows larger amplitude variations, data from the second epoch alone were used to create X-ray spectra with <3 count s^{-1} and >3 count s^{-1}.

A difference spectrum (high flux − low flux) was created to identify components that vary between the flux states. If changes between the flux levels were only due to changes in the normalization of the spectral components then a single power law should describe the difference spectrum well. Fitting the 3–10 keV band with a power law ($\Gamma = 2.00 \pm 0.16$) resulted in a good fit. Extrapolating the power law to 0.5 keV reveal a strong excess towards lower energies. Normalization changes may be responsible for the majority of variability in the broad-band spectra, although changes in the shape of the spectral components at lower energies may be important.

The two flux-resolved spectra were then fitted with the models for partial covering absorption, blurred reflection, and Comptonization to examine the origin of the rapid variability. In the absorption model, changes in X-ray flux could be caused by either the primary emitter or by the absorbing material. Two sources of ionized absorption explain the X-ray spectra best (Section 5.2), one with higher column density than the other. Geometrically, these could represent two distinct absorbing materials or a single absorber with a density gradient. Ionization could also vary across a single larger body as the material closer to incident radiation would experience more illumination than that on the far side. As absorbing material moves, overlaps, or condenses/disperses a spectrum can change. The simplest scenario assumes variability caused only by a change in covering fraction, with all other properties of the absorbers remaining constant.

Allowing only the covering fractions to vary between flux states in the ionized absorption model from Section 5.2 returned $\chi^2/\text{dof} = 909/768$ and moderate residual features. There was a small discrepancy in the spectra around 5 keV where the model overpredicted the low flux state and underpredicted the high flux state. In addition, only the covering fraction of the denser absorber changed significantly and so the model was revised. With the covering fraction of the denser absorber alone providing the variability, the fit statistic stayed approximately the same for an additional free parameter and the residuals diminished. The model described the data equally well if the column density of the denser absorber was allowed to vary with the covering fraction (Fig. 11). This scenario makes sense as two overlapping bodies would alter both the total covering fraction and column density along the line of sight.

A comparative fit was found when the power-law parameters alone were allowed free to vary between flux states. It was mentioned above how this scenario is much more difficult to justify: a change in the covering fraction could easily account for short-term variability on kilosecond time-scales, but it is challenging to imagine a mechanism that would force the slope of the power law to fluctuate so quickly. Therefore, the best explanation for the short-term variability using absorption is a partial covering model where a cloud of denser material is moving into the line of sight as another cloud with lower density continues to obscure the same solid angle.

A similar procedure was followed for testing the reflection scenario. From past analysis (Section 5.3), it appears that the X-ray spectra are power-law dominated and that changes in the normalization of the primary emitter itself drive most of the short-term variability (Fig. 10). As the primary emitter brightens or perhaps moves along the axis of rotation, the emissivity profile of the disc can alter (e.g. Gallo et al. 2013; Wilkins & Gallo 2015) and material at closer radii experiences a change in ionization. When considering the scenario of a moving 'lamp post' corona emitting isotropically, upward motion would decrease primary X-ray radiation on the inner disc and result in a harder, power-law-dominated X-ray spectrum. Downward motion of the corona would cause the disc to be illuminated anisotropically due to light bending, increasing the reflected flux from the inner region and producing a softer, reflection-dominated spectrum.
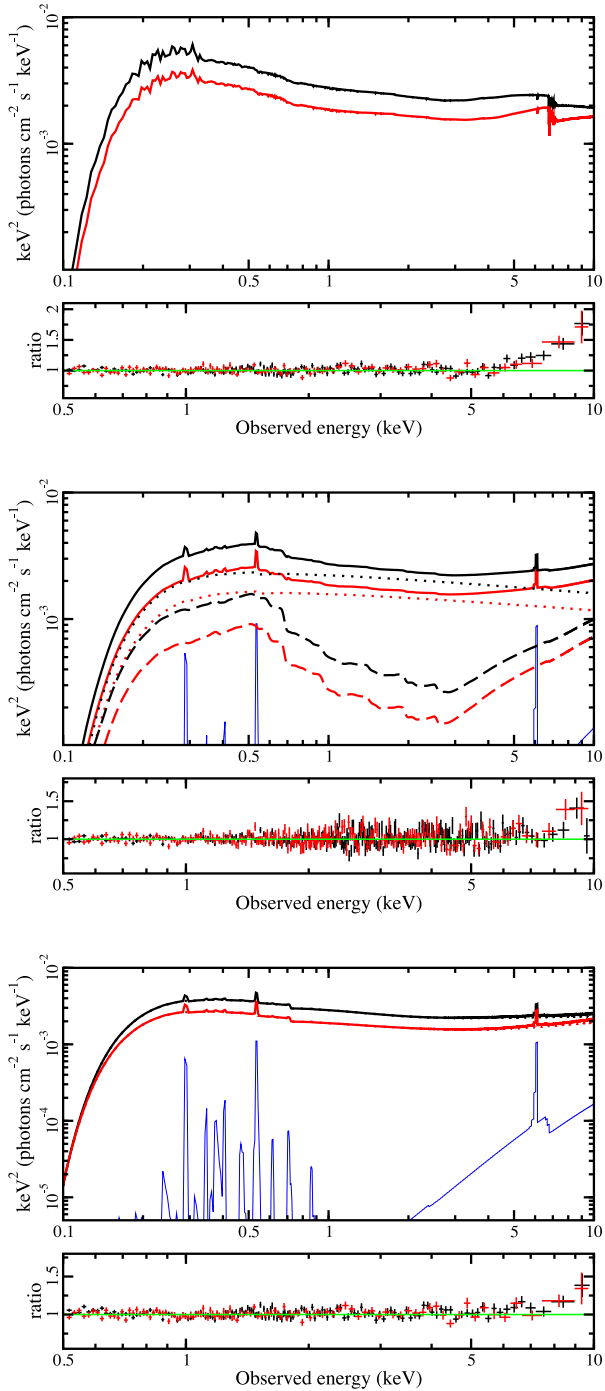
change can be attributed to changes in the power-law normalization, which seems consistent with the fractional variability and difference spectrum analysis. Subtle changes in the ionization parameter of the disc arise from changes in the illuminating flux, which can explain the low-energy excess in the difference spectrum.

Lastly, the soft Comptonization model (Section 5.4) was fit to the flux-resolved spectra with only the primary component (Γ) and the radius of the soft Comptonizing region (R_{cor}) allowed to vary. Further OPTXAGNF parameters were thawed gradually until the most reasonable model was found (Table 7). The model that gave the lowest χ_ν^2 value allowed R_{cor}, kT_e, τ, Γ, and f_{pl} all to vary; however, these parameters values were inconsistent with those from the average spectral fits. The soft Comptonization model that best describes the flux-resolved spectra in a manner consistent with the mean spectral fits allowed only R_{cor}, Γ, and f_{pl} to vary. This appears to support the scenario that changes in the primary component are responsible for short-term variability in this object: as the primary component changes over time, the fraction of the primary X-rays that are reprocessed in the soft Comptonizing region (f_{pl}) also changes, as does the radius of the soft Comptonizing region (R_{cor}).

The spectrum is dominated by a single component and the amplitude and spectral variation are modest in HE 0436–4717, thus making more complex timing analysis difficult to justify. That being said, a lag analysis was performed using three different energy bands for comparisons. Given the data quality, lags could only be constrained to within a few hundred seconds in each frequency band. There was no significant detection of a frequency-dependent lag (E. Cackett, private communication), but this could simply be a data quality issue.

7 DISCUSSION

The multi-epoch, multiband analysis of HE 0436–4717 has resulted in several scenarios that describe the spectra of the object equally well on a purely statistical basis. In the first interpretation, emission from the central engine passes through at least one ionized body of gas that absorbs the incident radiation. The spectrum produces an apparent SE that is an artefact of the absorption. The second scenario describes the X-ray emission as a composite of multiple sources. Here, the primary source from a compact 'lamp post' corona dominates over emission from blurred, ionized reflection and a distant, neutral reflector. The Fe Kα line seen in this case is a sum of the relativistically broadened iron line originating from the inner regions of the accretion disc and a narrow line from the distant reflector. The SE is a consequence of blurred ionized reflection from the inner regions of the accretion disc. Lastly, it could be that the X-ray spectra of HE 0436–4717 is composed of a primary component from a radially extended corona in a 'sandwich' configuration. The SE in this case is produced by a soft Comptonizing region in the inner disc and a distant reflector produces the Fe Kα line.

It is not unusual for these interpretations to model a spectrum equally well. Due to the complex nature of AGN, it is reasonable to assume that perhaps all three mechanisms (partial covering absorption, blurred reflection, and soft Comptonization) can be present in a single object. However, the degeneracy between the models can lead to confusion when attempting to reconstruct source geometry. Timing analysis can be key in determining the processes that are dominant at a given time. Variability in HE 0436–4717 is described well with reflection, as it appears that changes in flux of the primary emitter can be seen influencing both the short- and long-term behaviour of this object. Assuming an isotropic lamp-post corona, changes on kilosecond time-scales reflect an increase/decrease in primary

Figure 11. The partial covering (top), blurred reflection (middle), and soft Comptonization (bottom) models fit to the flux-reduced spectra with their respective residuals (data/model) shown below each. The high-flux data are black, low-flux are red. The distant reflector, as needed, is shown in blue. Increased residuals above 8 keV can likely be attributed to the reduced statistics and higher background in that band.

The reflection model from Section 5.3 was applied to the flux-resolved spectra (Fig. 11). A good fit could be achieved by allowing the power-law component to vary in shape and normalization and the blurred reflector to respond with changes in ionization (Table 7). Allowing other parameters, such as the reflector normalization or emissivity profile, to vary did not enhance the fit. Most of the

Table 7. Summary of models fit to the flux-resolved spectra. Column 1 lists the individual models and column 2 the model components. Note that only the soft Compton component of the total soft Compton model (Table 6) is shown for simplicity. The model parameters are shown in column 3 with their values for the high- and low-flux states listed in columns 4 and 5, respectively. Parameters linked across the epochs are denoted by dots and those without errors are frozen at the given values.

(1) Model	(2) Component	(3) Parameters	(4) High-flux state	(5) Low-flux state
Partial covering Absorption	Absorber 1	Γ	$2.40^{+0.04}_{-0.01}$	–
		$N_{\mathrm{H},1}$ (cm^{-2})	$51.17^{+7.67}_{-8.17}$	–
		CF_1	$0.62^{+0.05}_{-0.06}$	$0.74^{+0.03}_{-0.04}$
	Absorber 2	$N_{\mathrm{H},2}$ (cm^{-2})	$6.00^{+1.14}_{-1.44}$	–
		CF_2	$0.32^{+0.06}_{-0.03}$	–
		χ^2_ν/dof	1.18/769	
Blurred reflection	Primary power law	Γ	2.14 ± 0.01	2.12 ± 0.02
		$F_{0.1–100\,\mathrm{keV}}$	$2.17 \pm 0.04 \times 10^{-11}$	$1.55 \pm 0.04 \times 10^{-11}$
	Blurred reflection	α_{in}	5.67	–
		α_{out}	3.0	–
		$R_{\mathrm{br}}(R_g)$	6.0	–
		R_{in}	1.79	–
		θ (°)	43.5	–
		A_{Fe} (solar)	0.36	–
		Γ	$\Gamma_{\mathrm{primary}}$	–
		ξ (erg cm s^{-1})	72 ± 4	53 ± 3
		$F_{0.1–100\,\mathrm{keV}}$	$1.12 \pm 0.05 \times 10^{-11}$	$0.71 \pm 0.06 \times 10^{-11}$
	Reflection fraction	$\mathcal{R}$	0.52 ± 0.03	0.45 ± 0.04
	Distant reflector	A_{Fe} (solar)	1.0	–
		Γ	1.9	–
		ξ (erg cm s^{-1})	1.0	–
		χ^2_ν/dof	1.12/772	
Soft Comptonization	Soft Compton component	M_{BH} (M$_\odot$)	5.9×10^7	–
		D_{L} (Mpc)	233.1	–
		$\log(L/L_{\mathrm{Edd}})$	-1.05	–
		$\log R_{\mathrm{out}}$	3	–
		a	0.8	–
		R_{cor} (R_g)	$14.84^{+1.39}_{-1.12}$	$10.85^{+10.17}_{-1.34}$
		kT_{e} (keV)	$0.61^{+0.20}_{-0.11}$	–
		τ	$7.73^{+1.19}_{-1.27}$	–
		Γ	2.12 ± 0.01	$1.89^{+0.04}_{-0.03}$
		f_{pl}	0.54 ± 0.02	$0.44^{+0.05}_{-0.12}$
		χ^2_ν/dof	1.42/772	

X-ray flux with respect to the accretion disc. The changes in flux could either be intrinsic or due to the motion of the corona (e.g. Wilkins et al. 2014; Gallo et al. 2015), which in turn increases/decreases the ionization of the disc at inner radii. Over longer, multi-year time-scales fluctuations in power-law slope can be seen which would be caused by physical changes in the corona itself (i.e. an alteration in temperature and optical depth). HE 0436–4717 remains in a power-law-dominated state throughout the observed epochs. When looking at the broader picture of HE 0436–4717 and its behaviour, the blurred reflection interpretation is the most self-consistent model.

The preference for a reflection scenario in HE 0436–4717 leaves the challenge of explaining the persistently low iron abundance. Observations have shown that most AGN have solar to supersolar metallicity values independent of redshift (e.g. Storchi-Bergmann et al. 1998; Hamann et al. 2002). In several independent studies, it was shown that most AGN are also located in massive galaxies with classical bulges (Greene & Ho 2004; Barth, Greene & Ho 2005). As stellar mass is strongly correlated with metallicity (Tremonti et al. 2004), it is reasonable to expect the majority of AGN to thus have solar metallicity values or higher. The question then arises: under what circumstances would AGN be observed with (apparently) intrinsic sub-solar metallicities?

Groves, Heckman & Kauffmann (2006) set out to find such AGN and searched Sloan Digital Sky Survey observations of Seyfert 2 galaxies to find those that have sub-solar metallicities. Out of a sample of around 23 000 they found only ∼40 candidates based on optical line ratios from the narrow-line region (NLR). The authors suggest that most AGN are only observed after periods of intense star formation in their host galaxies and so the infalling gas supplying the central engine is already abundant with heavy elements. This implies that AGN with inherently sub-solar metals may somehow be feeding off gas that has yet to be processed by stars. It could be that HE 0436–4717 has an unusually low star formation rate for its redshift and/or less Type 1a supernovae to produce iron. Another possibility is that low-metallicity gas from outside of the galaxy has made its way to the central black hole either through a merger or filament, as in the scenarios proposed to explain the unusually low abundances in the NLR of radio-quiet quasar HE 2158–0107 (Husemann et al. 2011).

Other Seyfert 1 galaxies in particular have been known to show sub-solar iron abundances, such as NGC 4593 (Reynolds et al. 2004), NGC 3227, and 4051 (Patrick et al. 2012), and MCG+8-11-11 (Bianchi et al. 2010). Patrick et al. (2012) suggest that a persistently low abundance could represent a component of the Fe Kα line originating from a Compton thin material such as the broad-line region (BLR) or NLR. The full-width half-maximum (FWHM) of the iron line was calculated for both the pn and merged MOS spectra. The measured FWHM corresponded to velocities of $\sim$0.45 c and $\sim$0.31 c for pn and MOS, respectively. G10 measured the FWHM of the optical Hβ line in HE 0436–4717 and determined the BLR velocity to be around 3990 km s^{-1} or about 0.01 c. Thus, while the exact nature of the iron feature in HE 0436–4717 remains uncertain, it is clear that the line is not originating from the BLR but instead display disc-like velocities ($>$0.1 c, Miller 2007). A narrow iron feature from a distant reflector is also required to describe the data in this object. The narrow line could originate from the NLR, but it is unlikely that such a significant fraction of the radiation originates from the region (e.g. Kaspi, Brandt & George 2002; Fukazawa, Hiragi & Mizuno 2011).

Another alternative is the possibility of spallation reducing the reflected Fe Kα flux due to bombardment from high-energy ($>$10 MeV) protons. Skibo (1997) explains how abundances of sub-Fe metals between 4.5 and 6.4 keV can be enhanced in the nuclear regions of AGN at the expense of the Fe line. The author calculates the abundances of metals that could fall in the Fe Kα red-wing and finds that the corresponding fluxes (specifically those of Ti, V, Cr, and Mn) relative to Fe would be large enough to raise their lines above the continuum. The combined strength of these sub-Fe lines would be comparable to the strength of the Fe line from which these lines are produced. If this were the case in HE 0436–4717, additional features in the red-wing should be detected. In particular, Cr (at 5.4 keV) and Mn (at 5.9 keV) are predicted to have a combined flux $\sim$40–50 per cent that of the observed Fe Kα line – no such features are detected in the *XMM–Newton* spectra.

Finally, perhaps the intrinsic amount of iron in the central engine is not sub-solar, but the amount of other metals higher since the abundance of other metals in the spectral models is fixed at their respective solar values. The iron abundance in this object is low enough, however, that the other metals in the system would have to be supersolar in order to account for the apparent lack of iron. It is a challenge to determine a mechanism that would substantially increase other metals in a gas without affecting the iron, although a lack of Type Ia supernovae (mentioned previously) may do this. More specifically, a decrease in the ratio between Type Ia/Type II supernovae could decrease the relative abundance of iron as both produce the heavy metals that decay into iron, however Type Ia more efficiently disperse material into the surrounding interstellar medium (i.e. no supernova remnant remains).

The possibility of HE 0436–4717 having intrinsic sub-solar iron abundance is intriguing as such objects are rare. Deep analysis of the host galaxy would help to further constrain the metallicity of this object and also advance understanding of AGN-host relations.

8 CONCLUSIONS

A broad-band analysis of the Seyfert 1 galaxy HE 0436–4717, covering from optical up to 100 keV is presented. SED modelling suggests the source is unobscured and perhaps its black hole mass and distance could be better constrained. A reverberation mapping campaign would be advantageous to accurately determine the black hole mass in HE 0436–4717.

The multi-epoch X-ray spectra are fitted with Comptonization, blurred reflection, and partial covering models, but do not reveal a significantly preferred model. Consideration of the rapid variability favours a blurred reflection scenario where the variability is dominated by changes in the power-law normalization accompanied by corresponding changes in the disc ionization. However, the blurred reflection model indicates a very low iron abundance for HE 0436–4717. The low iron abundance does not seem to be an artefact of the modelling process, and abundances are not tested in the Comptonization or partial covering scenarios.

Observations of the host galaxy are limited, but would be beneficial to examine any abnormalities in the distribution of abundances in HE 0436–4717. Future X-ray observations with the calorimeter *Astro-H* (Takahashi et al. 2014) could also reveal narrow features in the X-ray spectra that would allow abundances to be better constrained. In addition to revealing narrow spectral features, *Astro-H* will also allow for simultaneous, broad-band soft and hard X-ray observations. This should remove some of the ambiguity that is currently present from utilizing BAT data alongside that from *XMM–Newton* .

REFERENCES

Barth A. J., Greene J. E., Ho L. C., 2005, ApJ, 619, L151
Baumgartner W. H., Tueller J., Markwardt C. B., Skinner G. K., Barthelmy S., Mushotzky R. F., Evans P. A., Gehrels N., 2013, ApJS, 207, 19
Bianchi S., de Angelis I., Matt G., La Parola V., de Rosa A., Grandi P., Jiménez Bailón E., Piconcelli E., 2010, A&A, 522, 64
Breeveld A. A. et al., 2010, MNRAS, 406, 1687
Burrows D. N. et al., 2005, Space Sci. Rev., 120, 165
Cusumano G. et al., 2010, A&A, 524, 64
Dauser T., Wilms J., Reynolds C. S., Brenneman L. W., 2010, MNRAS, 409, 1534
den Herder J. W. et al., 2001, A&A, 365, 7
Done C., Davis S. W., Jin C., Blaes O., Ward M., 2012, MNRAS, 420, 1848
Edelson R., Turner T. J., Pounds K., Vaughan S., Markowitz A., Marshall H., Dobbie P., Warwick R., 2002, ApJ, 568, 610
Elvis M., Plummer D., Schachter J., Fabbiano G., 1992, ApJS, 80, 257
Elvis M., Lockman F. J., Fassnacht C., 1994, ApJS, 95, 413
Emmanoulopoulos D., Papadakis I. E., McHardy I. M., Nicastro F., Bianchi S., Arévalo P., 2011, MNRAS, 415, 1895
Fabian A. C., Rees M. J., Stella L., White N. E., 1989, MNRAS, 238, 729
Fukazawa Y., Hiragi K., Mizuno M., 2011, ApJ, 727, 19
Gallo L. C., 2006, MNRAS, 368, 479
Gallo L. C. et al., 2013, MNRAS, 428, 1191
Gallo L. C. et al., 2015, MNRAS, 446, 633
García J., Dauser T., Reynolds C. S., Kallman T. R., McClintock J. E., Wilms J., Eikmann W., 2013, ApJ, 768, 146
Greene J. E., Ho L. C., 2004, ApJ, 610, 722
Groves B. A., Heckman T. M., Kauffmann G., 2006, MNRAS, 371, 1559
Grupe D., Beuermann K., Thomas H.-C., Mannheim K., Fink H. H., 1998, A&A, 330, 25

Grupe D., Komossa S., Leighly K. M., Page K. L., 2010, ApJS, 187, 64. (G10)

Halpern J., Marshall H. L., 1996, ApJ, 464, 760

Hamann F., Korista K. T., Ferland G. J., Warner C., Baldwin J., 2002, ApJ, 564, 592

Husemann B., Wisotzki L., Jahnke K., Sánchez S. F., 2011, A&A, 535, 72

Jansen F. et al., 2001, A&A, 365, L1

Jin C., Ward M., Done C., 2012, MNRAS, 425, 907

Kalberla P. M. W., Burton W. B., Hartmann D., Arnal E. M., Bajaja E., Morras R., Pöppel W. G. L., 2005, A&A, 440, 775

Kaspi S., Brandt W. N., George I. M., 2002, ApJ, 574, 643

Kubota A., Done C., 2004, MNRAS, 353, 980

Mason K. O. et al., 2001, A&A, 365, L36

Miller J. M., 2007, ARA&A, 45, 441

Nandra K., Pounds K. A., 1994, MNRAS, 268, 406

Patrick A. R., Reeves J. N., Porquet D., Markowitz A. G., Lobban A. P., Terashima Y., 2011, MNRAS, 411, 2353

Patrick A. R., Reeves J. N., Porquet D., Markowitz A. G., Braito V., Lobban A. P., 2012, MNRAS, 426, 2522

Ponti G., Cappi M., Dadina M., Malaguti G., 2004, A&A, 417, 451

Poole T. S. et al., 2008, MNRAS, 383, 627

Predehl P., Schmitt J. H. M. M., 1995, A&A, 293, 889

Reynolds C. S., 2013, Nature, 494, 432

Reynolds C. S., Brenneman L. W., Wilms J., Kaiser M. E., 2004, MNRAS, 352, 205

Roming P. W. A. et al., 2005, Space Sci. Rev., 120, 95

Ross R. R., Fabian A. C., 2005, MNRAS, 358, 211

Shimura T., Takahara F., 1995, ApJ, 445, 780

Skibo J. G., 1997, ApJ, 478, 522

Storchi-Bergmann T., Schmitt H. R., Calzetti D., Kinney A. L., 1998, AJ, 115, 909

Strüder L. et al., 2001, A&A, 365, L18

Takahashi T. et al., 2014, in Takahashi T., Jan-Willem den Herder A., Bautz M., eds, Proc. SPIE Conf. Ser. Vol. 9144, Space Telescopes and Instrumentation 2014: Ultraviolet to Gamma Ray. SPIE, Bellingham, p. 25

Tananbaum H. et al., 1979, ApJ, 234, L9

Titarchuk L., 1994, ApJ, 434, 70

Tremonti C. A. et al., 2004, ApJ, 613, 898

Turner T. J., Miller L., 2009, A&AR, 17, 47

Turner M. J. L. et al., 2001, A&A, 365, L27

Vagnetti F., Antonucci M., Trevese D., 2013, A&A, 550, 12

Vasudevan R. V., Fabian A. C., 2009, MNRAS, 392, 1124 (VF09)

Vasudevan R. V., Mushotzky R. F., Winter L. M., Fabian A. C., 2009, MNRAS, 399, 1553. (V09)

Vasudevan R. V., Mushotzky R. F., Reynolds C. S., Fabian A. C., Lohfink A. M., Zoghbi A., Gallo L. C., Walton D., 2014, ApJ, 785, 30

Vaughan S., Fabian A. C., Ballantyne D. R., De Rosa A., Piro L., Matt G., 2004, MNRAS, 351, 193

Vestergaard M., Peterson B. M., 2006, ApJ, 641, 689

Walton D. J., Nardini E., Fabian A. C., Gallo L. C., Reis R. C., 2013, MNRAS, 428, 2901

Wang T., Otani C., Matsuoka M., Cappi M., Leighly K. M., Brinkmann W., 1998, MNRAS, 293, 397

Wilkins D. R., Gallo L. C., 2015, MNRAS, 449, 129

Wilkins D. R., Kara E., Fabian A. C., Gallo L. C., 2014, MNRAS, 443, 2746

Wisotzki L., Christlieb N., Bade N., Beckmann V., Köhler T., Vanelle C., Reimers D., 2000, A&A, 358, 77.

Yaqoob T., Murphy K. D., Miller L., Turner T. J., 2010, MNRAS, 401, 411

This paper has been typeset from a TEX/LATEX file prepared by the author.